OPTICS

Ultrasensitive and long-range transverse displacement metrology with polarization-encoded metasurface

Haofeng Zang[1]†, Zheng Xi[1,2]†, Zhiyu Zhang[1]†, Yonghua Lu[1,2]*, Pei Wang[1,2]*

Copyright © 2022 The Authors, some rights reserved; exclusive licensee American Association for the Advancement of Science. No claim to original U.S. Government Works. Distributed under a Creative Commons Attribution NonCommercial License 4.0 (CC BY-NC).

A long-range, high-precision, and compact transverse displacement metrology method is of crucial importance in many research areas. Recent schemes using optical antennas are limited in efficiency and the range of measurement due to the small size of the antenna. Here, we demonstrated the first prototype polarization-encoded metasurface for ultrasensitive long-range transverse displacement metrology. The transverse displacement of the metasurface is encoded into the polarization direction of the outgoing light via the Pancharatnam-Berry phase, which can be read out directly according to the Malus law. We experimentally demonstrate nanometer displacement resolution with the uncertainty on the order of 100 picometers for a large measurement range of 200 micrometers with the total area of the metasurface being within 900 micrometers by 900 micrometers. The measurement range can be extended further using a larger metasurface. Our work opens new avenues of applying metasurfaces in the field of ultrasensitive optical transverse displacement metrology.

INTRODUCTION

Precise measurement of small displacements using optical methods is the main driving force behind many research areas such as gravitational wave detection (*1*), super-resolution microscopy (*2*), and semiconductor industry (*3*, *4*). Tremendous efforts have been made to continuously push the limits of optical displacement metrology: The most prominent example being the use of the large-scale optical interferometer with ultrahigh power (*1*) and with engineered quantum states of light whose noise can be suppressed below the classical limit (*5*). However, most interferometers such as Michelson/Mach-Zehnder setups are designed to measure the longitudinal displacement (the displacement direction is along the beam path) and are insensitive to the transverse displacement (the displacement direction is perpendicular to the beam path). Besides, the interferometer system is affected by the slight air disturbance in the measurement environment and the mechanical vibration of the instrument, which requires high environmental stability.

Recently, there is a growing interest in the field of nanophotonics to develop novel compact devices other than large-scale interferometers for transverse position sensing (*6*–*12*), which is especially important for applications in semiconductor industry and super-resolution microscopy where the room for placing the displacement sensor is rather limited. For instance, using the highly position-dependent directional scattering from an optical antenna placed inside a spatially tailored focused field, a localization precision on the order of subangstrom has been demonstrated (*8*, *11*). However, because the incident field is a highly focused field, this method suffers from the problem of a small measurement range, typically within hundreds of nanometers. The measurement range can be extended by considering periodically modulated structured light formed by two-wave interference (*7*, *9*), but the low scattering efficiency from the antenna puts a limit on the performance of such an approach. Recently, a long-range scheme was demonstrated using liquid crystal plates (*12*), but nanometer displacement sensitivity is hardly achieved because of the large pitch size (50 μm) of the liquid crystal sample. Further pitch reduction is challenging for liquid crystal fabrication. Moreover, the optical property of liquid crystal depends strongly on the environmental temperature, making it less suitable for stable and high precision metrology applications. Another approach using superoscillatory field has been demonstrated for ultrasensitive transverse metrology (*13*). This method relies on using the very large local wave number called superoscillations around the phase singularities to achieve nanoscale precision. However, it requires complicated postprocessing and phase reconstruction algorithms. In general, a metrology method with a high measurement precision, a relatively long working range, and a direct readout scheme is highly desired.

Metasurface has triggered a broad interest in the area of imaging (*14*–*17*), encryption (*18*, *19*), holography (*20*, *21*), and display (*22*, *23*) because of its ability to shape and control the wavefront with subwavelength unit cell. In contrast to the liquid crystal devices, the fabrication of the metasurface is highly compatible with the semiconductor lithography process, and a much smaller pitch size can be easily fabricated. In this work, we put forward a previously unknown approach for transverse displacement metrology using a polarization-encoded metasurface. When a linearly polarized light is displaced transversely with respect to this metasurface, its polarization direction is rotated because of different Pancharatnam-Berry (PB) phases (*24*–*26*) acquired by different circular polarization components. The amount of polarization rotation varies linearly over a large range as a function of the transverse displacement. By adding an analyzer at the output, the transverse displacement information can be read out directly via the Malus law. Experimentally, we have demonstrated nanometer displacement resolution with an uncertainty on the order of 100 pm. We note that this value is largely due to the environmental noise in the laboratory and should not be considered as the lower limit on the metasurface's performance. Our work paves the way for the ultrasensitive, long-range, and easy readout scheme for transverse position metrology using metasurfaces.

[1]Department of Optics and Optical Engineering, University of Science and Technology of China, Hefei, Anhui 230026, P. R. China. [2]Advanced Laser Technology Laboratory of Anhui Province, Hefei, Anhui 230026, P. R. China.
*Corresponding author. Email: yhlu@ustc.edu.cn (Y.L.); wangpei@ustc.edu.cn (P.W.)
†These authors contributed equally to this work.

RESULTS

Theoretical concept

We first consider two longitudinally cascaded PB metasurfaces along the z axis, which we refer to as the transmission-type (T-type) measurement scheme. Each metasurface is made of many subwavelength optical antennas with spatially varying optical axis $\theta(x)$ along the x direction. Relying on the PB phase, the building block of each metasurface performs the maximum conversion between circular polarizations of different handedness with an additional phase factor $e^{\pm 2i\theta(x)}$ as the half-wave plate condition is satisfied (fig. S1) (*24*, *27*, *28*). When two of these metasurfaces are cascaded along the z axis, each with a locally varying optical axis profile $\theta_1(x)$ and $\theta_2(x)$, the underlying polarization conversion process is described by LCP → $\text{RCP}e^{2i\theta_1(x)}$ → $\text{LCP}e^{-2i\theta_2(x)}e^{2i\theta_1(x)}$ and RCP → $\text{LCP}e^{-2i\theta_1(x)}$ → $\text{RCP}e^{2i\theta_2(x)}e^{-2i\theta_1(x)}$ where LCP and RCP denote the left and right circular polarizations, respectively. If we then consider a linearly x-polarized input light $\vec{E}_{\text{in}} = [1,0]^T$ propagating along the z axis with these two metasurfaces lying in the XY plane, there are different phase delays for the two circularly polarized components. As a result, the polarization of light after these two metasurfaces is rotated and can be written as

$$\mathbf{E}_{\text{trans}} = [\cos 2(\theta_2(x) - \theta_1(x)), \sin 2(\theta_2(x) - \theta_1(x))]^T \quad (1)$$

It is a locally varying linearly polarized field with the polarization direction depending on the spatial coordinate x.

Of particular interest is the case when $\theta_2(x)$ is a displaced copy of $\theta_1(x)$ and $\theta_1(x)$ is a linear function of x; i.e., $\theta_2(x) = \theta_1(x + \delta x)$ and $\theta_1(x) = ax$ with a being a constant. Under these conditions, the transmitted field in Eq. 1 is simply given by

$$\begin{aligned}\mathbf{E}_{\text{trans}} &= \left[\cos\left(2\frac{d\theta_1}{dx}\delta x\right), \sin\left(2\frac{d\theta_1}{dx}\delta x\right)\right]^T \\ &= [\cos(2a\delta x), \sin(2a\delta x)]^T \end{aligned} \quad (2)$$

Comparing this field with Eq. 1, it is clear that, for this particular case, the dependence on the spatial coordinate x is removed. Instead, the polarization direction of the outgoing light field is homogenous over x and is solely determined by the amount of displacement δx. For different amounts of displacement δx, the polarization direction rotates periodically at a period of π/a. Thus, the two metasurfaces together serve as an optical encoder, which encodes the relative displacement information δx into the polarization direction of the outgoing light. By inserting an analyzer at the output, the displacement information can be readout directly according to the Malus law.

Equivalently, these two metasurfaces together with the polarizer and the analyzer can be viewed as a locally varying polarizer and a locally varying analyzer as shown in Fig. 1A. When the incident light passes through the first metasurface, it becomes a locally varying linearly polarized field, and the local polarization direction is shown in the top left row in Fig. 1A. The second metasurface together with the analyzer shown in Fig. 1A serves as a locally varying linear analyzer that analyzes the local polarization direction of the field after metasurface 1. All the local polarization directions can be synchronously rotated by shifting only the metasurface along the x axis. When the two metasurfaces are perfectly aligned, the directions of the local polarizer and local analyzer match perfectly. Thus, all the light is transmitted as shown in the first row of Fig. 1B. As the two metasurfaces are displaced horizontally with respect to each other

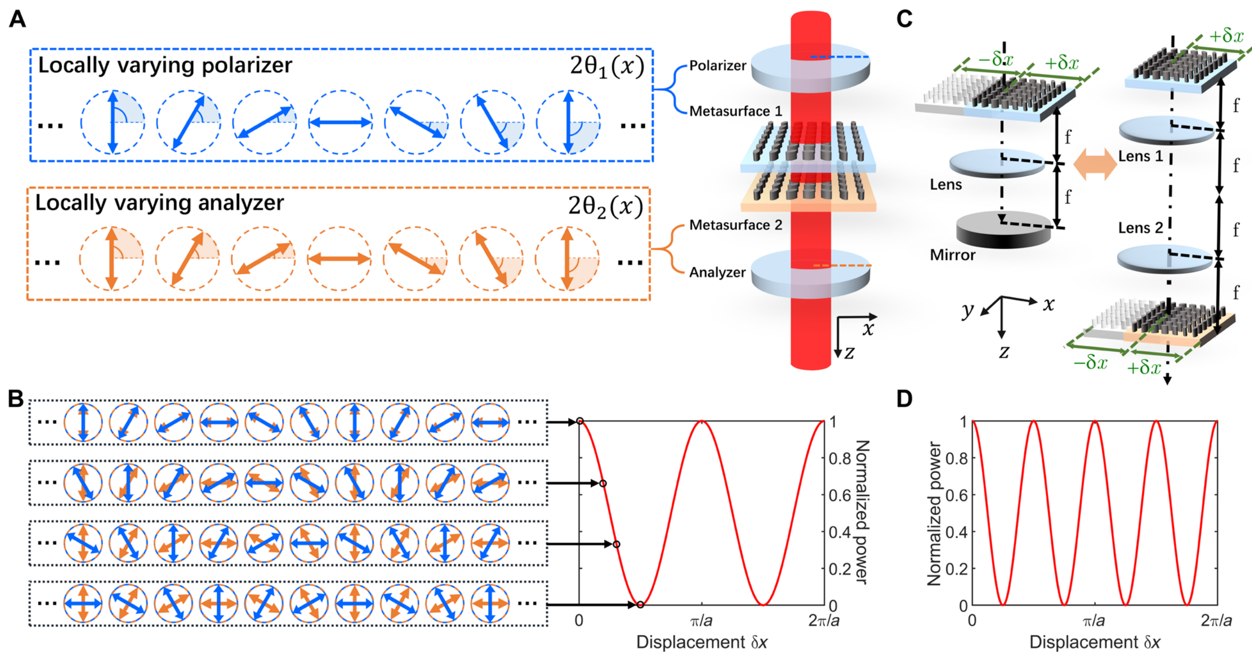

Fig. 1. Displacement sensing with PB metasurface in transmissive and reflective configuration. (**A**) The working principle of the T-type metasurface displacement sensor can be understood as the polarization match between the locally varying polarizer and the locally varying analyzer. The arrows indicate the polarization direction. (**B**) When the two metasurfaces are displaced with respect to each other, the output power changes periodically according to the Malus law. (**C**) The reflection-type (R-type) measurement scheme in which one measures the relative displacement of the metasurface with its image, which can be unfolded into the T-type. Note that the R-type scheme has doubled the sensitivity of the measurement. (**D**) Output power as a function of displacement for the R-type measurement scheme. Note that the sensitivity is doubled.

as shown in the second and third rows of Fig. 1B, the direction of the local polarizer and analyzer begin to mismatch gradually. As a result, the total output power decreases and goes to zero when the local directions of the two become orthogonally to each other, which is shown in the last row of Fig. 1B. The relative displacement can be read out directly by measuring the output power from the two elements according to the Malus law. For the conventional Malus law, it is used to describe the output power due to relative rotation between the polarizer and the analyzer with no information regarding to the relative displacement between the two. Here, by incorporating the PB metasurface design to create the locally varying polarizer and analyzer, we are able to extend the Malus law to readout the relative displacement.

We implement the above idea using a scheme shown in the left column of Fig. 1C. Instead of considering the displacement of two cascaded metasurfaces (T-type as shown in Fig. 1A), we use only one metasurface and a mirror and measure the displacement of one single metasurface relative to its own image [reflection-type (R-type) as shown in the left column of Fig. 1C]. This configuration offers additional benefits over the one shown in Fig. 1A: First, because the PB metasurface induces linear phase ramp of different signs to LCP/RCP, the output beams of LCP/RCP from the first metasurface in the T-type configuration are steered into different directions (fig. S2). As a consequence, the two metasurfaces should be placed very close to each other, which limit the practical applications (fig. S3). Second, the T-type scheme requires the two metasurfaces to be exactly the same, which is experimentally challenging. However, in the R-type configuration shown in the left column of Fig. 1C, the second metasurface is replaced by the image of the first metasurface (shaped one), and the "two" metasurfaces are the same and thus are free from the errors induced by the mismatch between the two metasurfaces. Third, the sensitivity of displacement measurement for the R-type scheme is doubled. To see this point in more detail, we consider unfolding the R-type configuration into a 4f T-type configuration shown in the right column of Fig. 1C. As stated above, the R-type configuration measures the displacement of the metasurface's image (shaded gray) with respect to itself (orange). As the object moves leftwards ($+\delta x$), the image moves rightwards ($-\delta x$). The relative displacement in this configuration is actually $2\delta x$, which is two times larger than the T-type case where only one of the metasurface is moving. As a result, if we now put an analyzer at the output, then the pitch of the measurement curve is half of the T-type as shown in Fig. 1D, and thus, the sensitivity is doubled.

Experiment

We design the optical properties of the Si optical antenna using finite-difference time-domain simulation (fig. S1). Each metasurface consists of these Si optical antennas with spatially varying optical axis sitting on a glass substrate. We fabricate three different metasurface samples using electron beam lithography (fig. S4) with pitch Λ ranging from 3 to 4.5 to 6 μm, and the conversion efficiencies of all the metasurface samples are high enough for the metrology applications.

Figure 2A shows a schematic illustration of our measurement setup. The inset on the bottom left of Fig. 2A shows the scanning electron microscopy (SEM) image of the sample with pitch $\Lambda = 3$ μm (fig. S5 for SEM images of other pitches). The stabilized light from the laser source gets linearly polarized after passing through the polarizer with very small power fluctuation (Fig. S6). A piezo stage is used to control the transverse displacement δx of the metasurface with respect to the center of the incident beam. After the PB metasurface, the incident linearly polarized light splits into two beams of LCP and RCP light of equal intensity, which carry different PB phases $e^{\pm 2i\theta} = e^{\pm i2a\delta x}$, where $a = \pi/\Lambda$. Because circular polarization reverses its handedness after reflection, a quarter–wave plate is inserted behind the lens to maintain the polarization handedness before and after the reflection from the mirror. The spatial filter is used to block the unmodulated background light that is directly

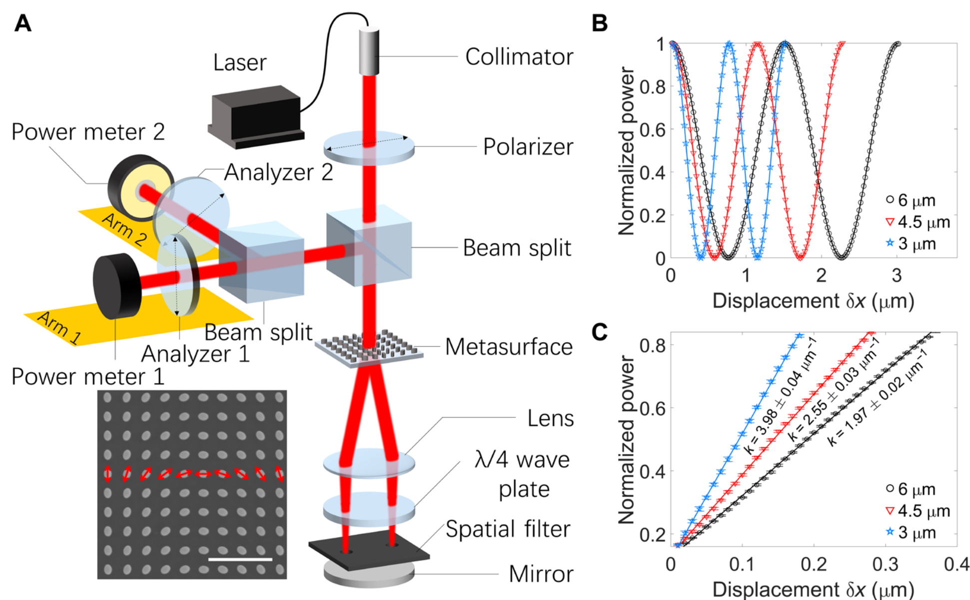

Fig. 2. Experimental realization of the PB metasurface displacement sensor. (**A**) Schematic illustration of the measurement setup. Inset: A SEM image of the sample with pitch $\Lambda = 3$ μm. The red arrows indicate the orientation of major axes of optical antenna. Scale bar, 1 μm. (**B**) Output power as at different metasurface locations for samples with pitches $\Lambda = 3$, 4.5, and 6 μm. It can be seen that the short pitch gives a higher slope and thus a higher sensitivity. (**C**) Linear regions of three curves in (B).

transmitted through the metasurface. After the reflected light passes through the metasurface again, the LCP and RCP components acquire an additional PB phase of $e^{\pm i2a\delta x}$ so that the overall phase difference is $8a\delta x$, and because the metasurface recombines the LCP and RCP component, the outgoing light is again linearly polarized but with the polarization direction rotated by $4a\delta x$. We use an analyzer and a power meter to read out this polarization rotation and thus the displacement δx. The additional power meter in arm 2 in Fig. 2A is used to detect the signal that is phase-shifted. This allows us to cover the full measurement cycle in a linear way as will be shown in the following discussions on the measurement range of the metasurface.

During the measurement, we first align the metasurface to the center of the optical axis. The metasurface is then scanned along the x direction with a step size of 5, 10, and 20 nm (fig. S7). For each position, we use a power meter to measure the output power within 1 s at the sampling frequency of 500 Hz. The averaged power as a function of position x is plotted in Fig. 2B. For each curve, the maximum power is normalized for better visualization. Here, we only show the measured results for the step size of 20 nm to demonstrate the large measurement range of our device.

The output power in Fig. 2B follows a sinusoidal pattern as predicted by the theoretical model, which can be fitted well by

$$P(\delta x) = P_0 \cos^2\left(\frac{4\pi}{\Lambda}\delta x\right) \quad (3)$$

where P_0 is the maximum output power from the metasurface and is normalized to 1. To quantify the sensitivity of our metasurface, we define the sensitivity as the absolute value of the slope of the curve, $s(\delta x) = \left|\frac{dP}{d\delta x}\right| = \frac{4\pi}{\Lambda}\left|\sin\left(\frac{8\pi}{\Lambda}\delta x\right)\right|$. It reaches the maximum value of $s_{\max} = \frac{4\pi}{\Lambda}$ at positions $\delta x = \frac{\Lambda}{16}m, m = 1,3,5\ldots$ We thus focus on these linear regions around which the sensitivity is the maximum as shown in Fig. 2C. The measured sensitivity k of the three samples are $k_{6\mu m} = 1.97\ \mu m^{-1}$, $k_{4.5\mu m} = 2.55\ \mu m^{-1}$, and $k_{3\mu m} = 3.98\ \mu m^{-1}$, respectively, which agrees well with the best theoretical sensitivity given by $s_{6\mu m} = 2.09\,\mu m^{-1}$, $s_{4.5\mu m} = 2.79\,\mu m^{-1}$, and $s_{3\mu m} = 4.19\,\mu m^{-1}$. The measured sensitivity is slightly lower than the theoretical one, because the theoretical value is taken at the point of the maximum sensitivity, whereas the measured sensitivity is averaged over the linear region. As expected, smaller pitch gives a high slope and thus a higher sensitivity to displacement. The demonstrated sensitivity is more than one order of magnitude higher than the previous case using liquid crystals (*12*) because of the notable decrease in the pitch size via metasurface design over the liquid crystal case. In the following discussions, we focus on the 3-μm pitch sample, as it provides the largest sensitivity.

Measurement resolution and precision

We quantify the measurement resolution and the precision of our measurement scheme. In Fig. 3A, we show the measurement results from the 3-μm sample at different measurement steps. Each red dot in Fig. 3A corresponds to the obtained normalized power from one measurement, and the horizontal black line indicates the movement of the piezo stage at the steps of 20, 10, and 5 nm in the three plots, respectively. It can be seen that a 10-nm step is clearly resolvable from the experimental data. However, for the step size of 5 nm, the obtained power fluctuation due to the intrinsic instability of the piezo stage approaches to the power difference arisen from the one-step movement.

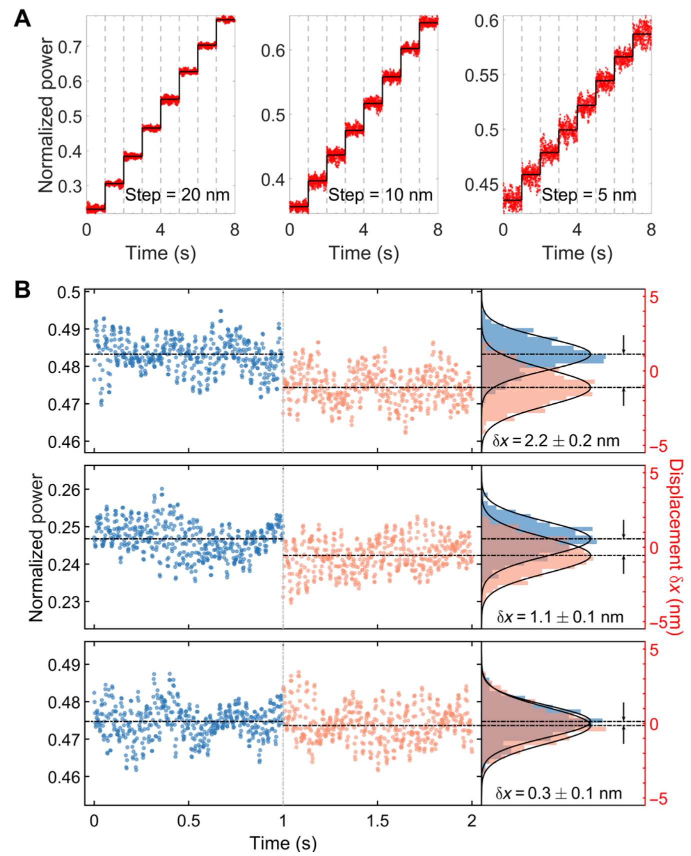

Fig. 3. Resolution and precision of the PB metasurface displacement sensor. (**A**) Deterministic measurement results from the 3-μm sample at different measurement steps of 20 nm (left), 10 nm (center), and 5 nm (right). (**B**) Statistics of the measurement power at different positions from the indeterministic measurement. The two positions are well resolved (top), just resolved (middle), and less resolved (bottom).

To solve this issue and quantify the best resolution for our PB metasurface measurement scheme, we repeatedly measure the displacement within the same linear region and look at the power difference from the two measurements. This measurement scheme provides us with a series of measurement outcomes. By raster scanning our metasurface samples within the linear region, it is possible that we end up with some positions that are closer than the minimum uncertainty and we can measure these positions to characterize the best performance of our metasurfaces. We refer this kind of measurement as the indeterministic measurement, which complements the above deterministic measurement via moving the piezo stage at deterministic fixed steps (*8*). Figure 3B shows the histograms of the normalized power distributions at three different positions. For each histogram, we take 500 points from the measurement and use a Gaussian function to fit the histogram (fig. S8). A relative displacement of 1 nm can be clearly resolved from the two peaks, which is limited by the width of Gaussian fitting of two measurements. For a displacement down to 3 Å, the distinction between the two positions is less obvious.

The Gaussian fit in Fig. 3B also allows us to infer the measurement precision of our metasurface scheme. The error σ_x in estimating the position x can be obtained via the following error propagation

$$\sigma_x = \delta x \sqrt{\left(\frac{\sqrt{(\sigma_{P1})^2 + (\sigma_{P2})^2}}{{P_1}^N - {P_2}^N}\right)^2 + \left(\frac{\sigma_k}{k}\right)^2} \quad (4)$$

where σ_{P1} and σ_{P2} are the SDs of the Gaussian fit with respect to the power distributions P_1^N and P_2^N, respectively. The superscript N indicates that all of the data points are normalized. σ_k is the SD of the linear fitting around the measurement's linear region as shown in Fig. 2C. Following this formula, we obtained σ_x = 0.2, 0.1, and 0.1 nm for the data shown in Fig. 3B, which is quite remarkable considering the environmental noise in the laboratory. This value due to environmental noise in the laboratory is almost the same for all the three metasurface samples as shown in the Supplementary Materials. We note that this value serves only as the upper limit for our measurement imprecision, by reducing the environmental noise using, for example, lock-in amplifier, a better measurement precision could be obtained. To corroborate the influence of the environment noise, we monitor the displacement caused by the environment noise throughout a whole night in two different days (fig. S10), and the details of the typical data analysis can be found in table S1. It can be seen that the system resolution of the same metasurface at different time has changed notably, which is mainly affected by environmental noise. The resolution is clearly higher in midnight because the people's activities calm down.

Measurement range

We demonstrate the ability of our metasurface for long-range displacement sensing. As can be seen from the above measurement results in Fig. 2B, there are regions where the measured power curve is quite flat, and these positions correspond to the "peaks and valleys" of the sinusoidal pattern. Around these regions, the sensitivity is almost zero, and we refer to these regions as the "dead regions" of our displacement sensor. For a long-range measurement, these dead regions should be avoided. To solve this issue, we add another power meter at the output and record the power in this arm (arm 2 in Fig. 2A) by rotating the analyzer by 45°. This corresponds to effectively shifting the measured signal in the original arm (arm 1 in Fig. 2A) such that the original peaks and valleys become the positions of the largest slope in the shifted component as shown in Fig. 4A. By cascading the linear regions of these two signals (fig. S9), we are able to extend the region of linearity to the full measurement range as shown in Fig. 4B. As a demonstration of our metasurface for long-range measurement, we scan our piezo stage at a step size of 100 nm at its full measurement range (200 μm). Figure 4C shows the measurement results for different displacement segments sampled from the full range. It can be seen that our metasurface can perform a long-range displacement measurement. In addition, note that the size of the metasurface serves as a limiting factor for the long-range measurement. For a larger displacement, the overlapping area between metasurface and its image decreases; thus, the effective modulation area decreases as well (fig. S3). This effect can also be observed from Fig. 4C, where the middle sinusoidal curve has the maximum peak power, which corresponds to the largest overlap. As the metasurface and its image are displaced, the overlapping area decreases, and therefore, the maximum peak power of the two sinusoidal curves on the left and on the right in Fig. 4C decreases. As an

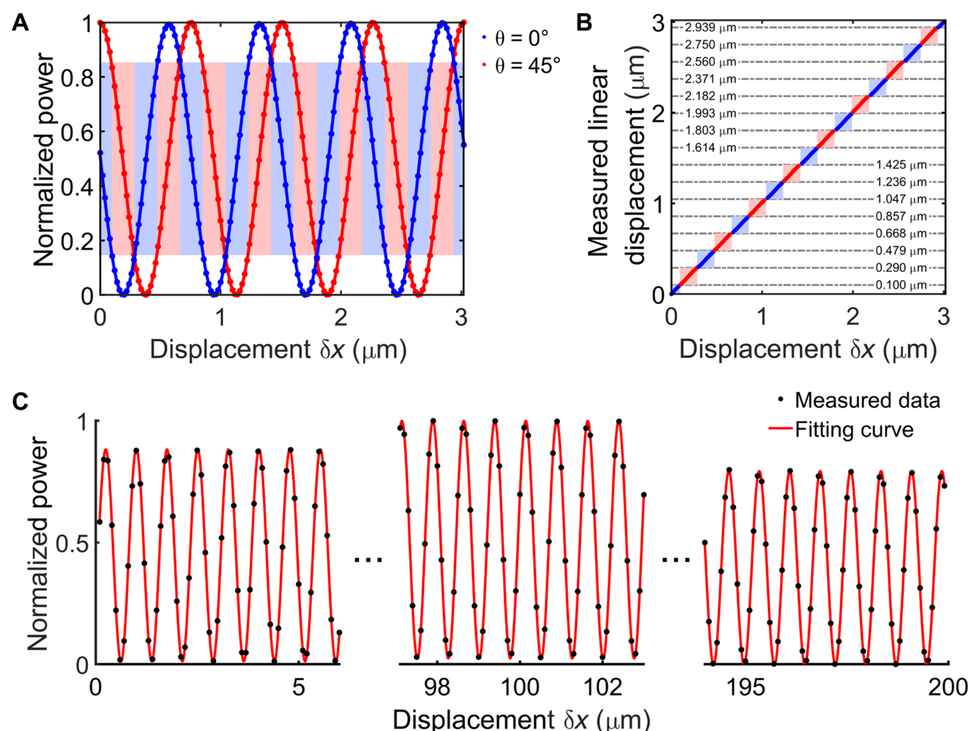

Fig. 4. Realization of a long-range linear measurement. (**A**) Full coverage of the linear regions via detection of the two signals that are phase shifted with each other at the output as shown in Fig. 2A. Light red/blue area in the background indicates the linear region of the red/blue curve. (**B**) The linear measurement results covering the full measurement cycle by stitching the linear regions in (A). The gray dashed line indicates the displacement at the stitching point. (**C**) Segments from measurement in which range covers all piezo stage movement range with a 100-nm step. In each segment, the measured data can fit well with the sine curve. The difference in power in different segments is due to the change in the overlapping area of the metasurface and its image as shown in Fig. 1C.

estimation of the measurement range of the current metasurface sample, we set the critical overlapping area as the half of the area of the metasurface sample (overall size of 900 μm by 900 μm). This gives us an estimated measurement range from −450 to 450 μm. This value can be further extended using larger metasurface samples.

DISCUSSION

In summary, we have proposed and demonstrated an ultrasensitive transverse displacement measurement scheme based on PB metasurface. The displacement information is encoded in the polarization direction of the output light. Using Malus law, the transverse displacement can be stably read out very precisely within nanometer resolution with an uncertainty on the order of 100 pm. We argue that this is largely due to the environment noise in our laboratory. Using a high-power laser with ultrastable output and advanced measurement schemes such as lock-in amplifier or homodyne detection, the measurement precision can be pushed further. We note that a higher sensitivity refers to a larger change in the measured power for a given displacement, while the measurement precision is mainly determined by the environmental noise in our setup. A higher sensitivity can be particularly important when the detector's power resolution is moderate. That is, smaller pitch metasurface displacement sensor can play an important role in the development of low-cost metrology sensors, because the need for a high-performance detector can be balanced via higher displacement sensitivity.

Our scheme has a large measurement range on the order of several hundreds of micrometers, which can be extended by using a larger metasurface sample. This value is at least three orders of magnitude larger than the metrology schemes involving optical antennas (*8*, *11*) whose measurement range is typically on the order of the wavelength, yet our method achieved similar resolution. Considering the implementations, the metasurface sample can be easily packed into a box that can be attached to the side of the measurement target such as a moving stage. One may extend to in-plane two-dimensional displacement measurements, as different channels can be potentially used for encoding information about displacements along both x and y dimensions (*29*). Our work opens new avenues for using metasurfaces for transverse displacement sensing and may find important applications in the areas of semiconductor industry and super-resolution microscopy where the precise information of the transverse displacement is a must.

MATERIALS AND METHODS

Design of metasurface

The Jones matrix of the elliptical nanoantenna constituting each metasurface is given by (*27*, *30*)

$$J(\theta) = \eta_1 I + \eta_2 (e^{i2\theta} |R\rangle\langle L| + e^{-i2\theta} |L\rangle\langle R|) \tag{5}$$

Here, the kets $|R\rangle = \begin{pmatrix}1\\ i\end{pmatrix}$ and $|L\rangle = \begin{pmatrix}1\\ -i\end{pmatrix}$ denote RCP and LCP, respectively, and the bras $\langle R|$ and $\langle L|$ are their conjugate transpose. I is a 2 by 2 identity matrix. $|R\rangle\langle L|$ and $|L\rangle\langle R|$ refer to the conversion between RCP and LCP. The complex coefficient $\eta_1 = \frac{1}{2}(t_o e^{i\varphi_o} + t_e e^{i\varphi_e})$ indicates the amplitude transmittance of the incident circular polarization, and $\eta_2 = \frac{1}{2}(t_o e^{i\varphi_o} - t_e e^{i\varphi_e})$ represents the conversion efficiency between LCP and RCP, where t_o and t_e are amplitude transmittances, and φ_o and φ_e are phase delays for the incidence polarization along the o axis and e axis. θ is the orientation of the optical axis of the antenna.

To achieve a complete conversion between RCP and LCP, a half-wave plate condition $t_o = t_e$ and $|\varphi_o - \varphi_e| = \pi$ (fig. S1C) is imposed during the design process. In this case, the Jones matrix can be simplified as

$$J(\theta) = e^{i2\theta} |R\rangle\langle L| + e^{-i2\theta} |L\rangle\langle R| \tag{6}$$

For the x-polarized incidence $|E_{\text{in}}\rangle = \begin{pmatrix}1\\ 0\end{pmatrix} = \frac{1}{2}(|R\rangle + |L\rangle)$, the outgoing light field is

$$|E_{\text{out}}\rangle = J|E_{\text{in}}\rangle = \frac{1}{2}(e^{i2\theta}|R\rangle + e^{-i2\theta}|L\rangle) \tag{7}$$

It contains two orthogonal polarization components with an opposite phase delay, which only depends on the orientation θ. For $\theta(x) = \pi\frac{x}{\Lambda}$ where Λ is the period, the different outgoing circular polarization components experience difference phase ramp and are refracted to opposite directions (fig. S2). In addition, Eq. 7 can be simplified as

$$|E_{\text{out}}\rangle = \frac{1}{2}\left(e^{i2\theta}\begin{pmatrix}1\\ i\end{pmatrix} + e^{-i2\theta}\begin{pmatrix}1\\ -i\end{pmatrix}\right) = \left[\cos 2\pi\frac{x}{\Lambda}, -\sin 2\pi\frac{x}{\Lambda}\right]^T \tag{8}$$

which presents a homogenous intensity electric field with spatially varying polarization (fig. S3C).

In our design, the incident light passes through two same metasurfaces with a transverse displacement δx. The outgoing light field is

$$|E_{\text{out}}\rangle = J(\theta_2)J(\theta_1)|E_{\text{in}}\rangle = \frac{1}{2}(e^{i2(\theta_2-\theta_1)}|R\rangle + e^{-i2(\theta_2-\theta_1)}|L\rangle) \tag{9}$$

where $\theta_1 = \pi\frac{x}{\Lambda}$ and $\theta_2 = \pi\frac{x+\delta x}{\Lambda}$. The above equation also can be simplified to

$$|E_{\text{out}}\rangle = [\cos 2(\theta_2-\theta_1), \sin 2(\theta_2-\theta_1)]^T = \left[\cos 2\pi\frac{\delta x}{\Lambda}, \sin 2\pi\frac{\delta x}{\Lambda}\right]^T \tag{10}$$

It is obvious that the output light is a homogenous field, and the polarization is exclusively determined by δx.

Simulation

Optical simulations were performed with finite-difference time-domain method. The refractive indexes of α-Si and glass substrate were respectively set as 3.88 + 0.0189i (*31*) and 1.46 at a wavelength of 633 nm. To meet the half-wave plate condition at 633 nm, the height (H), major axis length (D_o), and minor axis length (D_e) of the Si nanoantenna are chosen as H = 410 nm, D_o = 152 nm, and D_e = 104 nm during the simulation. The simulation area was 300 nm by 300 nm by 1600 nm with periodic boundary along x and y directions and perfectly matched layer boundary along the z direction. The plane wave incident light was set within the substrate and more than λ/2 away from the antenna along the z axis. The amplitude and phase of transmitted light were recorded with monitors in the air. The eligible antenna was selected to be the basic cell of the metasurface. For the polarization-encoded metasurface, supercell (Λ = 3 μm) containing 10 space-variant nanoantennas along the x axis was adopted to replace the Si antenna unit above; meanwhile, the simulation area, source, and monitors were enlarged correspondingly. A xz plane monitor was added to record the propagation of the light.

Fabrication

The metasurface sample is fabricated using the standard electron beam lithography (fig. S5). First, the 410-nm-thick α-Si film is grown on the fused quartz substrate by the plasma-enhanced chemical vapor deposition. The refractive index of Si is $3.88 + 0.0195i$ at a wavelength of 633 nm (measured by Ellipsometer, Sopra, GES5E). Subsequently, a 120-nm-thick negative electron beam resist [Hydrogen Silsesquioxane (HSQ), XR-1541.006] layer is spin coating on it (soft bake temperature, 100°C for 4 min). Then, the metasurface pattern is defined in the resist by electron beam lithography (JEOL-6300FS) with a 100-kV acceleration voltage and a beam current of 500 pA. Next, the resist is developed by 25% tetramethylammonium hydroxide solution for about 120 s to reveal the pattern. Last, the pattern is transferred to α-Si film by the inductively coupled plasma system (ICP380, Oxford). The residual resist is removed by buffered oxide etch solution.

Experimental instrument

As shown in Fig. 2A, the laser (MRL-III-633L-80mW) is bought from Changchun New Industries Optoelectronics Technology Co. Ltd. The collimator is Thorlabs F110FC-633. The output beam waist diameter is 1.16 mm, which is larger than the metasurface size of 900 μm, so the incident light intensity on the metasurface is spatially uniform. The piezo electric stage is Physik Instrumente P-545.3C8S with a resolution of 1 nm. The lens is Thorlabs AC254-050-A-ML. The optical power meter used is Thorlabs S120VC with PM400. We tested the stability of the experimental system as shown in fig. S4. The laser power without the metasurface modulation is stable enough during one measurement period (1 s) with the relative error of 0.01%.

Characterization of the metasurface sample

The polarization conversion efficiency η_2 of all the three metasurface samples was measured experimentally. A linearly polarized laser irradiates the metasurface sample from the substrate, and the refracted LCP and RCP light intensity is measured by the optical power meter and added together. As a comparison, the same laser passing through the pure glass substrate is also measured. The intensity conversion efficiency $|\eta_2|^2$ is obtained by dividing the total intensity of the transmitted LCP and RCP light over the light intensity after the glass substrate, which is 36.8% for the sample with pitch $\Lambda = 3$ μm, 47.4% for the sample with pitch $\Lambda = 4.5$ μm, and 67.4% for the sample with pitch $\Lambda = 6$ μm, respectively. All the intensity conversion efficiencies are high enough for the displacement metrology, although they are notably smaller than the simulated conversion efficiency of around 80% (fig. S1B). The deterioration of the conversion efficiency can be mainly attributed to the fabrication imperfection and the unavoidable deviation between the simulation and real sample.

The polarization conversion is also verified by checking the polarization state of the refracted light after the metasurface. The polarization state of the output light is determined by measuring the Stokes parameters of the light with a polarimeter (Thorlabs, PAX1000VIS) (fig. S2B). The ellipticity η, defined as the ratio of the minor axis length to the major axis length of the polarization ellipse, is calculated according to the measured Stokes parameters. For the LCP incident light ($S_1 = 0$, $S_2 = 0$, and $S_3 = -1$ and $\eta = 1$), the Stokes parameters of output light are $S_1 = -0.09$, $S_2 = 0.07$, and $S_3 = 0.99$, and the ellipticity is $\eta = 0.891$ (0.888 for simulation), which is evidently regarded as RCP light. Correspondingly, for the RCP incident light ($S_1 = 0$, $S_2 = 0$, and $S_3 = 1$ and $\eta = 1$), the Stokes parameters of the output refracted light are $S_1 = 0.02$, $S_2 = -0.1$, and $S_3 = -0.99$, and the ellipticity is $\eta = 0.902$ (0.873 for simulation), which is very close to LCP.

Data acquisition and uncertainty analysis

The displacement sensing experiment was implemented by three metasurface samples with periods of 3, 4.5, and 6 μm, respectively. For each sample, the displacement sensing was taken in three different steps of 5, 10, and 20 nm repeatedly, and the metasurface was moved by 200 steps in every measurement (fig. S7). At each position, the output optical signal was recording by the power meter within 1 s at the sampling frequency of 500 Hz. The power meter works in a high-resolution, low-sampling rate measurement mode to keep a relatively low level of electronic noise. The measured power P is normalized according to the formula $(P - P_{\min})/(P - P_{\min})_{\max}$. Then, we make a histogram of the data points at each location and set the number of bins to $[\sqrt{n}]$, where n is the number of data measured at that location and [...] is rounded to the nearest integer. Fitting the data by Gaussian distribution function, we get the fitting coefficients center P^N with SD σ_P and width W. The linear region is the region where the normalized power P is between $P^N_{l-\min} = (2-\sqrt{2})/4$ and $P^N_{l-\max} = (2+\sqrt{2})/4$ (=0.14 to 0.86). $P^N_{l-\min}$ and $P^N_{l-\max}$ are intersections of two ideal signal curves in Eq. 3 with π/4 as the phase difference and the subscript l indicates the linear region. The sensitivity k with SD σ_k is the slope by linear fitting.

We repeatedly measured the displacement of the linear region with a 10-nm step and observed the position difference retrieved from the two measurements data. P^N_1 and P^N_2 are the normalized fitting coefficients center of Gaussian fitting of the two-measurement data, respectively. Intensity changes come from the relative displacement in the x direction, with $\delta x = \left(P^N_1 - P^N_2\right)/k$. We show the histograms of different δx for samples with periods of 3, 4.5, and 6 μm (fig. S8). It is seen that the displacement can still be clearly distinguished at 1.1 nm. The width of the Gaussian distribution, which is mainly caused by the vibration of the external environment, limits the just resolved relative displacement of the system. The measurement results at different time are shown in fig. S10 and highlighted in table S1. To evaluate resolving ability of the system at different time, resolving ability R is calculated, which is defined as the ratio of the average width $\overline{W}$ and the slope k of the linear region. Before midnight (the front three lines in table S1), the measurement period becomes longer because of the drift of the sample, which, in turn, makes the slope smaller. Meanwhile, environmental vibration will make the Gaussian fitting width larger. The result is a decline in the resolving ability of the system. After midnight (the later four lines in table S1), the period measurement error and fitting width caused by environmental noise are smaller, so the system has a better resolving ability. When the environmental vibration can be effectively suppressed, the resolving ability of the system can be better.

Then, we use the error transfer function to calculate uncertainty of the relative displacement Δx, which has the form $f = A/B$. In this case, relative displacement $\delta x = \left(P^N_1 - P^N_2\right)/k$, and hence

$$A = P^N_1 - P^N_2, \quad B = k \tag{11}$$

We calculate σ_{P1} and σ_{P2} that are the SDs of the Gaussian fitting center of P^N_1 and P^N_2, respectively. The two measurements are independent of each other, and hence

$$\sigma_A = \sqrt{(\sigma_{P1})^2 + (\sigma_{P2})^2} \text{ for } A = P^N_1 - P^N_2, \quad \sigma_B = \sigma_k \text{ for } B = k \tag{12}$$

Then, we use the error transfer function to calculate uncertainty of δx as follows

$$\begin{aligned}\sigma_x &= \sigma_{A/B} \\ &= \frac{A}{B}\sqrt{\left(\frac{\sigma_A}{A}\right)^2 + \left(\frac{\sigma_B}{B}\right)^2} \\ &= \delta x\sqrt{\left(\frac{\sqrt{(\sigma_{P1})^2 + (\sigma_{P2})^2}}{P_1^N - P_2^N}\right)^2 + \left(\frac{\sigma_k}{k}\right)^2}\end{aligned} \quad (13)$$

The σ_x for all three samples is 0.1 or 0.2 nm (fig. S8).

SUPPLEMENTARY MATERIALS

Supplementary material for this article is available at https://science.org/doi/10.1126/sciadv.add1973

REFERENCES AND NOTES

1. B. P. Abbott, R. Abbott, T. D. Abbott, M. R. Abernathy, F. Acernese, K. Ackley, C. Adams, T. Adams, P. Addesso, R. X. Adhikari, V. B. Adya, C. Affeldt, M. Agathos, K. Agatsuma, N. Aggarwal, O. D. Aguiar, L. Aiello, A. Ain, P. Ajith, B. Allen, A. Allocca, P. A. Altin, S. B. Anderson, W. G. Anderson, K. Arai, M. A. Arain, M. C. Araya, C. C. Arceneaux, J. S. Areeda, N. Arnaud, K. G. Arun, S. Ascenzi, G. Ashton, M. Ast, S. M. Aston, P. Astone, P. Aufmuth, C. Aulbert, S. Babak, P. Bacon, M. K. M. Bader, P. T. Baker, F. Baldaccini, G. Ballardin, S. W. Ballmer, J. C. Barayoga, S. E. Barclay, B. C. Barish, D. Barker, F. Barone, B. Barr, L. Barsotti, M. Barsuglia, D. Barta, J. Bartlett, M. A. Barton, I. Bartos, R. Bassiri, A. Basti, J. C. Batch, C. Baune, V. Bavigadda, M. Bazzan, B. Behnke, M. Bejger, C. Belczynski, A. S. Bell, C. J. Bell, B. K. Berger, J. Bergman, G. Bergmann, C. P. L. Berry, D. Bersanetti, A. Bertolini, J. Betzwieser, S. Bhagwat, R. Bhandare, I. A. Bilenko, G. Billingsley, J. Birch, R. Birney, O. Birnholtz, S. Biscans, A. Bisht, M. Bitossi, C. Biwer, M. A. Bizouard, J. K. Blackburn, C. D. Blair, D. G. Blair, R. M. Blair, S. Bloemen, O. Bock, T. P. Bodiya, M. Boer, G. Bogaert, C. Bogan, A. Bohe, P. Bojtos, C. Bond, F. Bondu, R. Bonnand, B. A. Boom, R. Bork, V. Boschi, S. Bose, Y. Bouffanais, A. Bozzi, C. Bradaschia, P. R. Brady, V. B. Braginsky, M. Branchesi, J. E. Brau, T. Briant, A. Brillet, M. Brinkmann, V. Brisson, P. Brockill, A. F. Brooks, D. A. Brown, D. D. Brown, N. M. Brown, C. C. Buchanan, A. Buikema, T. Bulik, H. J. Bulten, A. Buonanno, D. Buskulic, C. Buy, R. L. Byer, M. Cabero, L. Cadonati, G. Cagnoli, C. Cahillane, J. C. Bustillo, T. Callister, E. Calloni, J. B. Camp, K. C. Cannon, J. Cao, C. D. Capano, E. Capocasa, F. Carbognani, S. Caride, J. C. Diaz, C. Casentini, S. Caudill, M. Cavaglià, F. Cavalier, R. Cavalieri, G. Cella, C. B. Cepeda, L. C. Baiardi, G. Cerretani, E. Cesarini, R. Chakraborty, T. Chalermsongsak, S. J. Chamberlin, M. Chan, S. Chao, P. Charlton, E. Chassande-Mottin, H. Y. Chen, Y. Chen, C. Cheng, A. Chincarini, A. Chiummo, H. S. Cho, M. Cho, J. H. Chow, N. Christensen, Q. Chu, S. Chua, S. Chung, G. Ciani, F. Clara, J. A. Clark, F. Cleva, E. Coccia, P.-F. Cohadon, A. Colla, C. G. Collette, L. Cominsky, M. Constancio Jr., A. Conte, L. Conti, D. Cook, T. R. Corbitt, N. Cornish, A. Corsi, S. Cortese, C. A. Costa, M. W. Coughlin, S. B. Coughlin, J.-P. Coulon, S. T. Countryman, P. Couvares, E. E. Cowan, D. M. Coward, M. J. Cowart, D. C. Coyne, R. Coyne, K. Craig, J. D. E. Creighton, T. D. Creighton, J. Cripe, S. G. Crowder, A. M. Cruise, A. Cumming, L. Cunningham, E. Cuoco, T. D. Canton, S. L. Danilishin, S. D'Antonio, K. Danzmann, N. S. Darman, C. F. D. S. Costa, V. Dattilo, I. Dave, H. P. Daveloza, M. Davier, G. S. Davies, E. J. Daw, R. Day, S. De, D. De Bra, G. Debreczeni, J. Degallaix, M. De Laurentis, S. Deléglise, W. Del Pozzo, T. Denker, T. Dent, H. Dereli, V. Dergachev, R. T. De Rosa, R. De Rosa, R. De Salvo, S. Dhurandhar, M. C. Díaz, L. Di Fiore, M. Di Giovanni, A. Di Lieto, S. Di Pace, I. Di Palma, A. Di Virgilio, G. Dojcinoski, V. Dolique, F. Donovan, K. L. Dooley, S. Doravari, R. Douglas, T. P. Downes, M. Drago, R. W. P. Drever, J. C. Driggers, Z. Du, M. Ducrot, S. E. Dwyer, T. B. Edo, M. C. Edwards, A. Effler, H.-B. Eggenstein, P. Ehrens, J. Eichholz, S. S. Eikenberry, W. Engels, R. C. Essick, T. Etzel, M. Evans, T. M. Evans, R. Everett, M. Factourovich, V. Fafone, H. Fair, S. Fairhurst, X. Fan, Q. Fang, S. Farinon, B. Farr, W. M. Farr, M. Favata, M. Fays, H. Fehrmann, M. M. Fejer, D. Feldbaum, I. Ferrante, E. C. Ferreira, F. Ferrini, F. Fidecaro, L. S. Finn, I. Fiori, D. Fiorucci, R. P. Fisher, R. Flaminio, M. Fletcher, H. Fong, J.-D. Fournier, S. Franco, S. Frasca, F. Frasconi, M. Frede, Z. Frei, A. Freise, R. Frey, V. Frey, T. T. Fricke, P. Fritschel, V. V. Frolov, P. Fulda, M. Fyffe, H. A. G. Gabbard, J. R. Gair, L. Gammaitoni, S. G. Gaonkar, F. Garufi, A. Gatto, G. Gaur, N. Gehrels, G. Gemme, B. Gendre, E. Genin, A. Gennai, J. George, L. Gergely, V. Germain, A. Ghosh, A. Ghosh, S. Ghosh, J. A. Giaime, K. D. Giardina, A. Giazotto, K. Gill, A. Glaefke, J. R. Gleason, E. Goetz, R. Goetz, L. Gondan, G. González, J. M. G. Castro, A. Gopakumar, N. A. Gordon, M. L. Gorodetsky, S. E. Gossan, M. Gosselin, R. Gouaty, C. Graef, P. B. Graff, M. Granata, A. Grant, S. Gras, C. Gray, G. Greco, A. C. Green, R. J. S. Greenhalgh, P. Groot, H. Grote, S. Grunewald, G. M. Guidi, X. Guo, A. Gupta, M. K. Gupta, K. E. Gushwa, E. K. Gustafson, R. Gustafson, J. J. Hacker, B. R. Hall, E. D. Hall, G. Hammond, M. Haney, M. M. Hanke, J. Hanks, C. Hanna, M. D. Hannam, J. Hanson, T. Hardwick, J. Harms, G. M. Harry, I. W. Harry, M. J. Hart, M. T. Hartman, C.-J. Haster, K. Haughian, J. Healy, J. Heefner, A. Heidmann, M. C. Heintze, G. Heinzel, H. Heitmann, P. Hello, G. Hemming, M. Hendry, I. S. Heng, J. Hennig, A. W. Heptonstall, M. Heurs, S. Hild, D. Hoak, K. A. Hodge, D. Hofman, S. E. Hollitt, K. Holt, D. E. Holz, P. Hopkins, D. J. Hosken, J. Hough, E. A. Houston, E. J. Howell, Y. M. Hu, S. Huang, E. A. Huerta, D. Huet, B. Hughey, S. Husa, S. H. Huttner, T. Huynh-Dinh, A. Idrisy, N. Indik, D. R. Ingram, R. Inta, H. N. Isa, J.-M. Isac, M. Isi, G. Islas, T. Isogai, B. R. Iyer, K. Izumi, M. B. Jacobson, T. Jacqmin, H. Jang, K. Jani, P. Jaranowski, S. Jawahar, F. Jiménez-Forteza, W. W. Johnson, N. K. J.-M. Daniel, D. I. Jones, R. Jones, R. J. G. Jonker, L. Ju, K. Haris, C. V. Kalaghatgi, V. Kalogera, S. Kandhasamy, G. Kang, J. B. Kanner, S. Karki, M. Kasprzack, E. Katsavounidis, W. Katzman, S. Kaufer, T. Kaur, K. Kawabe, F. Kawazoe, F. Kéfélian, M. S. Kehl, D. Keitel, D. B. Kelley, W. Kells, R. Kennedy, D. G. Keppel, J. S. Key, A. Khalaidovski, F. Y. Khalili, I. Khan, S. Khan, Z. Khan, E. A. Khazanov, N. Kijbunchoo, C. Kim, J. Kim, K. Kim, N.-G. Kim, N. Kim, Y.-M. Kim, E. J. King, P. J. King, D. L. Kinzel, J. S. Kissel, L. Kleybolte, S. Klimenko, S. M. Koehlenbeck, K. Kokeyama, S. Koley, V. Kondrashov, A. Kontos, S. Koranda, M. Korobko, W. Z. Korth, I. Kowalska, D. B. Kozak, V. Kringel, B. Krishnan, A. Królak, C. Krueger, G. Kuehn, P. Kumar, R. Kumar, L. Kuo, A. Kutynia, P. Kwee, B. D. Lackey, M. Landry, J. Lange, B. Lantz, P. D. Lasky, A. Lazzarini, C. Lazzaro, P. Leaci, S. Leavey, E. O. Lebigot, C. H. Lee, H. K. Lee, H. M. Lee, K. Lee, A. Lenon, M. Leonardi, J. R. Leong, N. Leroy, N. Letendre, Y. Levin, B. M. Levine, T. G. F. Li, A. Libson, T. B. Littenberg, N. A. Lockerbie, J. Logue, A. L. Lombardi, L. T. London, J. E. Lord, M. Lorenzini, V. Loriette, M. Lormand, G. Losurdo, J. D. Lough, C. O. Lousto, G. Lovelace, H. Lück, A. P. Lundgren, J. Luo, R. Lynch, Y. Ma, T. M. Donald, B. Machenschalk, M. M. Innis, D. M. Macleod, F. Magaña-Sandoval, R. M. Magee, M. Mageswaran, E. Majorana, I. Maksimovic, V. Malvezzi, N. Man, I. Mandel, V. Mandic, V. Mangano, G. L. Mansell, M. Manske, M. Mantovani, F. Marchesoni, F. Marion, S. Márka, Z. Márka, A. S. Markosyan, E. Maros, F. Martelli, L. Martellini, I. W. Martin, R. M. Martin, D. V. Martynov, J. N. Marx, K. Mason, A. Masserot, T. J. Massinger, M. Masso-Reid, F. Matichard, L. Matone, N. Mavalvala, N. Mazumder, G. Mazzolo, R. M. Carthy, D. E. M. Clelland, S. M. Cormick, S. C. M. Guire, G. M. Intyre, J. M. Iver, D. J. M. Manus, S. T. M. Williams, D. Meacher, G. D. Meadors, J. Meidam, A. Melatos, G. Mendell, D. Mendoza-Gandara, R. A. Mercer, E. Merilh, M. Merzougui, S. Meshkov, C. Messenger, C. Messick, P. M. Meyers, F. Mezzani, H. Miao, C. Michel, H. Middleton, E. E. Mikhailov, L. Milano, J. Miller, M. Millhouse, Y. Minenkov, J. Ming, S. Mirshekari, C. Mishra, S. Mitra, V. P. Mitrofanov, G. Mitselmakher, R. Mittleman, A. Moggi, M. Mohan, S. R. P. Mohapatra, M. Montani, B. C. Moore, C. J. Moore, D. Moraru, G. Moreno, S. R. Morriss, K. Mossavi, B. Mours, C. M. Mow-Lowry, C. L. Mueller, G. Mueller, A. W. Muir, A. Mukherjee, D. Mukherjee, S. Mukherjee, N. Mukund, A. Mullavey, J. Munch, D. J. Murphy, P. G. Murray, A. Mytidis, I. Nardecchia, L. Naticchioni, R. K. Nayak, V. Necula, K. Nedkova, G. Nelemans, M. Neri, A. Neunzert, G. Newton, T. T. Nguyen, A. B. Nielsen, S. Nissanke, A. Nitz, F. Nocera, D. Nolting, M. E. N. Normandin, L. K. Nuttall, J. Oberling, E. Ochsner, J. O'Dell, E. Oelker, G. H. Ogin, J. J. Oh, S. H. Oh, F. Ohme, M. Oliver, P. Oppermann, R. J. Oram, B. O'Reilly, R. O'Shaughnessy, C. D. Ott, D. J. Ottaway, R. S. Ottens, H. Overmier, B. J. Owen, A. Pai, S. A. Pai, J. R. Palamos, O. Palashov, C. Palomba, A. Pal-Singh, H. Pan, Y. Pan, C. Pankow, F. Pannarale, B. C. Pant, F. Paoletti, A. Paoli, M. A. Papa, H. R. Paris, W. Parker, D. Pascucci, A. Pasqualetti, R. Passaquieti, D. Passuello, B. Patricelli, Z. Patrick, B. L. Pearlstone, M. Pedraza, R. Pedurand, L. Pekowsky, A. Pele, S. Penn, A. Perreca, H. P. Pfeiffer, M. Phelps, O. Piccinni, M. Pichot, M. Pickenpack, F. Piergiovanni, V. Pierro, G. Pillant, L. Pinard, I. M. Pinto, M. Pitkin, J. H. Poeld, R. Poggiani, P. Popolizio, A. Post, J. Powell, J. Prasad, V. Predoi, S. S. Premachandra, T. Prestegard, L. R. Price, M. Prijatelj, M. Principe, S. Privitera, R. Prix, G. A. Prodi, L. Prokhorov, O. Puncken, M. Punturo, P. Puppo, M. Pürrer, H. Qi, J. Qin, V. Quetschke, E. A. Quintero, R. Quitzow-James, F. J. Raab, D. S. Rabeling, H. Radkins, P. Raffai, S. Raja, M. Rakhmanov, C. R. Ramet, P. Rapagnani, V. Raymond, M. Razzano, V. Re, J. Read, C. M. Reed, T. Regimbau, L. Rei, S. Reid, D. H. Reitze, H. Rew, S. D. Reyes, F. Ricci, K. Riles, N. A. Robertson, R. Robie, F. Robinet, A. Rocchi, L. Rolland, J. G. Rollins, V. J. Roma, J. D. Romano, R. Romano, G. Romanov, J. H. Romie, D. Rosińska, S. Rowan, A. Rüdiger, P. Ruggi, K. Ryan, S. Sachdev, T. Sadecki, L. Sadeghian, L. Salconi, M. Saleem, F. Salemi, A. Samajdar, L. Sammut, L. M. Sampson, E. J. Sanchez, V. Sandberg, B. Sandeen, G. H. Sanders, J. R. Sanders, B. Sassolas, B. S. Sathyaprakash, P. R. Saulson, O. Sauter, R. L. Savage, A. Sawadsky, P. Schale, R. Schilling, J. Schmidt, P. Schmidt, R. Schnabel, R. M. S. Schofield, A. Schönbeck, E. Schreiber, D. Schuette, B. F. Schutz, J. Scott, S. M. Scott, D. Sellers, A. S. Sengupta, D. Sentenac, V. Sequino, A. Sergeev, G. Serna, Y. Setyawati, A. Sevigny, D. A. Shaddock, T. Shaffer, S. Shah, M. S. Shahriar, M. Shaltev, Z. Shao, B. Shapiro, P. Shawhan, A. Sheperd, D. H. Shoemaker, D. M. Shoemaker, K. Siellez, X. Siemens, D. Sigg, A. D. Silva, D. Simakov, A. Singer, L. P. Singer, A. Singh, R. Singh, A. Singhal, A. M. Sintes, B. J. J. Slagmolen, J. R. Smith, M. R. Smith, N. D. Smith, R. J. E. Smith, E. J. Son, B. Sorazu, F. Sorrentino, T. Souradeep, A. K. Srivastava, A. Staley, M. Steinke, J. Steinlechner, S. Steinlechner, D. Steinmeyer, B. C. Stephens, S. P. Stevenson, R. Stone, K. A. Strain, N. Straniero, G. Stratta, N. A. Strauss, S. Strigin, R. Sturani, A. L. Stuver, T. Z. Summerscales, L. Sun, P. J. Sutton, B. L. Swinkels, M. J. Szczepańczyk, M. Tacca, D. Talukder, D. B. Tanner, M. Tápai, S. P. Tarabrin, A. Taracchini, R. Taylor, T. Theeg, M. P. Thirugnanasambandam, E. G. Thomas, M. Thomas, P. Thomas, K. A. Thorne, K. S. Thorne, E. Thrane, S. Tiwari, V. Tiwari, K. V. Tokmakov, C. Tomlinson, M. Tonelli,

C. V. Torres, C. I. Torrie, D. Töyrä, F. Travasso, G. Traylor, D. Trifirò, M. C. Tringali, L. Trozzo, M. Tse, M. Turconi, D. Tuyenbayev, D. Ugolini, C. S. Unnikrishnan, A. L. Urban, S. A. Usman, H. Vahlbruch, G. Vajente, G. Valdes, M. Vallisneri, N. van Bakel, M. van Beuzekom, J. F. J. van den Brand, C. Van Den Broeck, D. C. Vander-Hyde, L. van der Schaaf, J. V. van Heijningen, A. A. van Veggel, M. Vardaro, S. Vass, M. Vasúth, R. Vaulin, A. Vecchio, G. Vedovato, J. Veitch, P. J. Veitch, K. Venkateswara, D. Verkindt, F. Vetrano, A. Viceré, S. Vinciguerra, D. J. Vine, J.-Y. Vinet, S. Vitale, T. Vo, H. Vocca, C. Vorvick, D. Voss, W. D. Vousden, S. P. Vyatchanin, A. R. Wade, L. E. Wade, M. Wade, S. J. Waldman, M. Walker, L. Wallace, S. Walsh, G. Wang, H. Wang, M. Wang, X. Wang, Y. Wang, H. Ward, R. L. Ward, J. Warner, M. Was, B. Weaver, L.-W. Wei, M. Weinert, A. J. Weinstein, R. Weiss, T. Welborn, L. Wen, P. Weßels, T. Westphal, K. Wette, J. T. Whelan, S. E. Whitcomb, D. J. White, B. F. Whiting, K. Wiesner, C. Wilkinson, P. A. Willems, L. Williams, R. D. Williams, A. R. Williamson, J. L. Willis, B. Willke, M. H. Wimmer, L. Winkelmann, W. Winkler, C. C. Wipf, A. G. Wiseman, H. Wittel, G. Woan, J. Worden, J. L. Wright, G. Wu, J. Yablon, I. Yakushin, W. Yam, H. Yamamoto, C. C. Yancey, M. J. Yap, H. Yu, M. Yvert, A. Zadrożny, L. Zangrando, M. Zanolin, J.-P. Zendri, M. Zevin, F. Zhang, L. Zhang, M. Zhang, Y. Zhang, C. Zhao, M. Zhou, Z. Zhou, X. J. Zhu, M. E. Zucker, S. E. Zuraw, J. Zweizig; LIGO Scientific Collaboration and Virgo Collaboration, Observation of gravitational waves from a binary black hole merger. *Phys. Rev. Lett.* **116**, 061102 (2016).

2. B. Huang, M. Bates, X. Zhuang, Super-resolution fluorescence microscopy. *Annu. Rev. Biochem.* **78**, 993–1016 (2009).
3. A. J. den Boef, Optical wafer metrology sensors for process-robust CD and overlay control in semiconductor device manufacturing. *Surf. Topogr.* **4**, 023001 (2016).
4. N. G. Orji, M. Badaroglu, B. M. Barnes, C. Beitia, B. D. Bunday, U. Celano, R. J. Kline, M. Neisser, Y. Obeng, A. E. Vladar, Metrology for the next generation of semiconductor devices. *Nat. Electron.* **1**, 532–547 (2018).
5. H. Vahlbruch, S. Chelkowski, B. Hage, A. Franzen, K. Danzmann, R. Schnabel, Demonstration of a squeezed-light-enhanced power- and signal-recycled Michelson interferometer. *Phys. Rev. Lett.* **95**, 211102 (2005).
6. Z. Xi, L. Wei, A. J. L. Adam, H. P. Urbach, L. Du, Accurate feeding of nanoantenna by singular optics for nanoscale translational and rotational displacement sensing. *Phys. Rev. Lett.* **117**, 113903 (2016).
7. Z. Xi, H. P. Urbach, Magnetic dipole scattering from metallic nanowire for ultrasensitive deflection sensing. *Phys. Rev. Lett.* **119**, 053902 (2017).
8. A. Bag, M. Neugebauer, P. Woźniak, G. Leuchs, P. Banzer, Transverse kerker scattering for angstrom localization of nanoparticles. *Phys. Rev. Lett.* **121**, 193902 (2018).
9. L. Wei, A. V. Zayats, F. J. Rodríguez-Fortuño, Interferometric evanescent wave excitation of a nanoantenna for ultrasensitive displacement and phase metrology. *Phys. Rev. Lett.* **121**, 193901 (2018).
10. Z. Xi, S. Konijnenberg, H. P. Urbach, Information-efficient metagrating for transverse-position metrology. *Phys. Rev. Appl.* **14**, 014026 (2020).
11. T. Zang, H. Zang, Z. Xi, J. Du, H. Wang, Y. Lu, P. Wang, Asymmetric excitation of surface plasmon polaritons via paired slot antennas for angstrom displacement sensing. *Phys. Rev. Lett.* **124**, 243901 (2020).
12. R. Barboza, A. Babazadeh, L. Marrucci, F. Cardano, C. de Lisio, V. D'Ambrosio, Ultra-sensitive measurement of transverse displacements with structured light. *Nat. Commun.* **13**, 180 (2022).
13. G. H. Yuan, N. I. Zheludev, Detecting nanometric displacements with optical ruler metrology. *Science* **364**, 771–775 (2019).
14. R. J. Lin, V. C. Su, S. Wang, M. K. Chen, T. L. Chung, Y. H. Chen, H. Y. Kuo, J. W. Chen, J. Chen, Y. T. Huang, J. H. Wang, C. H. Chu, P. C. Wu, T. Li, Z. Wang, S. Zhu, D. P. Tsai, Achromatic metalens array for full-colour light-field imaging. *Nat. Nanotechnol.* **14**, 227–231 (2019).
15. W. T. Chen, A. Y. Zhu, V. Sanjeev, M. Khorasaninejad, Z. Shi, E. Lee, F. Capasso, A broadband achromatic metalens for focusing and imaging in the visible. *Nat. Nanotechnol.* **13**, 220–226 (2018).
16. M. Khorasaninejad, W. T. Chen, R. C. Devlin, J. Oh, A. Y. Zhu, F. Capasso, Metalenses at visible wavelengths: Diffraction-limited focusing and subwavelength resolution imaging. *Science* **352**, 1190–1194 (2016).
17. N. A. Rubin, G. D'Aversa, P. Chevalier, Z. Shi, W. T. Chen, F. Capasso, Matrix Fourier optics enables a compact full-Stokes polarization camera. *Science* **365**, eaax1839 (2019).
18. L. Deng, J. Deng, Z. Guan, J. Tao, Y. Chen, Y. Yang, D. Zhang, J. Tang, Z. Li, Z. Li, S. Yu, G. Zheng, H. Xu, C. Qiu, S. Zhang, Malus-metasurface-assisted polarization multiplexing. *Light Sci. Appl.* **9**, 101 (2020).
19. G. Qu, W. Yang, Q. Song, Y. Liu, C. Qiu, J. Han, D. Tsai, S. Xiao, Reprogrammable meta-hologram for optical encryption. *Nat. Commun.* **11**, 5484 (2020).
20. H. Ren, X. Fang, J. Jang, J. Bürger, J. Rho, S. A. Maier, Complex-amplitude metasurface-based orbital angular momentum holography in momentum space. *Nat. Nanotechnol.* **15**, 948–955 (2020).
21. H. Ren, G. Briere, X. Fang, P. Ni, R. Sawant, S. Héron, S. Chenot, S. Vézian, B. Damilano, V. Brändli, S. A. Maier, P. Genevet, Metasurface orbital angular momentum holography. *Nat. Commun.* **10**, 2986 (2019).
22. W. Joo, J. Kyoung, M. Esfandyarpour, S. Lee, H. Koo, S. Song, Y. Kwon, S. H. Song, J. C. Bae, A. Jo, M. Kwon, S. H. Han, S. Kim, S. Hwang, M. L. Brongersma, Metasurface-driven OLED displays beyond 10,000 pixels per inch. *Science* **370**, 459–463 (2020).
23. G. Lee, J. Hong, S. Hwang, S. Moon, H. Kang, S. Jeon, H. Kim, J. Jeong, B. Lee, Metasurface eyepiece for augmented reality. *Nat. Commun.* **9**, 4562 (2018).
24. Z. E. Bomzon, G. Biener, V. Kleiner, E. Hasman, Space-variant Pancharatnam-Berry phase optical elements with computer-generated subwavelength gratings. *Opt. Lett.* **27**, 1141–1143 (2002).
25. M. V. Berry, The adiabatic phase and Pancharatnam's phase for polarized light. *J. Mod. Opt.* **34**, 1401–1407 (1987).
26. S. Pancharatnam, Generalized theory of interference and its applications. *Proc. Indian Acad. Sci. A* **44**, 398–417 (1956).
27. D. Lin, P. Fan, E. Hasman, M. L. Brongersma, Dielectric gradient metasurface optical elements. *Science* **345**, 298–302 (2014).
28. A. Arbabi, Y. Horie, M. Bagheri, A. Faraon, Dielectric metasurfaces for complete control of phase and polarization with subwavelength spatial resolution and high transmission. *Nat. Nanotechnol.* **10**, 937–943 (2015).
29. Y. Yuan, K. Zhang, B. Ratni, Q. Song, X. Ding, Q. Wu, S. N. Burokur, P. Genevet, Independent phase modulation for quadruplex polarization channels enabled by chirality-assisted geometric-phase metasurfaces. *Nat. Commun.* **11**, 4186 (2020).
30. C. Menzel, C. Rockstuhl, F. Lederer, Advanced Jones calculus for the classification of periodic metamaterials. *Phys. Rev. A* **82**, 053811 (2010).
31. E. D. Palik, Silicon (amorphous), *in Handbook of Optical Constants of Solids* (Academic Press, 1997), vol. 3, pp. 571–586.

Acknowledgments: The nanofabrication was carried out at the USTC Center for Micro- and Nanoscale Research and Fabrication. **Funding:** This work was supported by National Key Research and Development Program of China (2020YFB2007501) and National Natural Science Foundation of China (U20A20216 and 62105320), and Z.X. is also financially supported by USTC starting grant (KY2030000143). **Author contributions:** P.W. and Y.L. conceived the ideas for this research and supervised the research. Z.Z. designed the metasurface and performed the fabrication. H.Z. set up the optical system and carried out the optical measurements and data processing. Z.X. and Y.L. wrote the manuscript and assisted in developing theoretical models and data analysis. H.Z. and Z.Z. wrote the Supplementary Materials. All the authors discussed the results, commented on the manuscript, and agreed on its final content. **Competing interests:** The authors declare that they have no competing interests. **Data and materials availability:** All data needed to evaluate the conclusions in the paper are present in the paper and/or the Supplementary Materials.

Submitted 26 May 2022
Accepted 24 August 2022
Published 12 October 2022
10.1126/sciadv.add1973